

Broadband Achromatic Metalens for the Short-Wave Infrared

¹ School of Physics and Astronomy, University of Glasgow, Glasgow G12 8QQ, UK

*y.he.5@research.gla.ac.uk

†adetunmise.dada@glasgow.ac.uk

Abstract: The 1.8-2.3 μm band lies within the short-wavelength infrared (SWIR) region and serves as a key operational window for a wide range of applications, including quantum sensing, molecular spectroscopy, and free-space quantum and classical optical communication. Despite its significance, optical devices operating in this band still face two major challenges: chromatic aberration across the wide spectral range and the difficulty of integration due to bulky optical elements. Metalenses are composed of subwavelength nanostructures that locally control the phase and group delay of light, enabling precise wavefront shaping and broadband dispersion compensation. These capabilities make them highly promising for use in infrared optical systems, particularly in applications such as focusing and imaging for compact integrated devices.

In this study, we propose a metalens design based on a CaF_2 substrate, where each nanocell consists of a single-bar silicon structure. These nanocells are periodically arranged with a 900 nm period, enabling precise control of dispersion and phase. By systematically finetuning the bar length and width, the design enables simultaneous dispersion compensation and phase modulation, achieving stable focusing performance over a broad spectral range. Finite-Difference Time-Domain (FDTD) simulations demonstrate that the metalens design achieves effective suppression of chromatic aberration in the 1800-2300 nm range, maintaining a stable focal position throughout the bandwidth with variation within 6% of the focal length. This design offers a compact, broadband, and high-performance approach for beam collimation and wavefront shaping in the SWIR band, showing promising potential for applications in quantum communication and sensing systems.

1. Introduction

1.1. Background

The short-wave infrared (SWIR) band generally refers to the spectral range of 1-2.5 μm [1]. Specific sub-bands around 2.1-2.2 μm coincide with an atmospheric transmission window [2], where absorption by water vapor and carbon dioxide is relatively weak compared with adjacent bands. Therefore, they bypass the strong absorption of water vapor and carbon dioxide. As a result, SWIR light exhibits relatively low atmospheric absorption and superior environmental adaptability [3, 4]. Compared with visible light, SWIR shows stable propagation in complex

environments such as haze and smoke [5, 6], which helps reduce scattering and losses. SWIR also maintains good imaging and detection capability even under low light or partial obstruction [7, 8].

In addition, some materials exhibit unique absorption or emission responses in this wavelength range [9–12], further enhancing system sensitivity and imaging quality. These properties make SWIR technologies widely applied in fields such as industrial inspection [13], material identification [14, 15], and biomedical imaging [16, 17]. Moreover, due to its partial penetration capability for certain non-transparent materials, SWIR is also extensively used in remote sensing [18, 19], meteorological observation [20], atmospheric composition analysis [21]. In optical communication, the SWIR band is suitable for free-space communication and short-distance data transmission owing to its robust environmental tolerance and favorable transmission characteristics [22]. In the field of quantum information, this band exhibits strong potential for medium- to long-distance quantum communication. Its advantages are particularly evident in free-space quantum links operating under complex or interference-prone conditions [23, 24]. Accordingly, it carries significant implications for both fundamental research and practical engineering applications.

Although the short-wave infrared (SWIR) band exhibits excellent environmental adaptability and broad application potential, the key optical component systems supporting its performance remain relatively underdeveloped, particularly at the micro-nano optics level. Quantum communication systems demand increasingly stringent performance from optical components [25, 26]. Devices must ensure stable wavefronts to suppress excess phase noise and achieve low dispersion with minimal wavefront distortion, thereby ensuring high-fidelity transmission of quantum states. However, current SWIR-compatible compact optical components still fall short of meeting these high-performance demands, especially in terms of wavefront control, dispersion management, and system integration adaptability. The further development of quantum systems is still hindered by factors such as large device dimensions, insufficient tuning precision, and the trade-off between miniaturization and environmental robustness. Despite progress in SWIR optics, micro-/nano devices still trail visible and NIR technologies in design flexibility and engineering practicality. Significant challenges still remain in design flexibility and engineering feasibility [27, 28], posing technical bottlenecks for their integration into high-precision quantum communication systems.

Compared with conventional optical elements, metalenses provide a promising solution to current limitations, because of their compact structure, high design flexibility, and outstanding performance in dispersion engineering and wavefront control [29, 30]. Broadband dispersion-compensating metalenses designed for the SWIR band show strong potential. They can meet the complex performance demands of advanced optical systems. Moreover, they support deeper integration of SWIR optics into quantum communication and photonic platforms.

As an emerging class of metasurface-based devices, metalenses have attracted widespread attention across multiple spectral bands in recent years due to their ultrathin profiles, high design flexibility, and multifunctional capabilities such as wavefront control and dispersion compensation. Initially developed for efficient focusing in the visible regime, their applications have gradually expanded into the near-infrared (NIR) and mid-infrared (MIR) domains (Fig. 1), encompassing imaging, spectroscopy, polarization manipulation, and other functions. Researchers have continually introduced material platforms such as TiO_2 [31], Si [32], and GaN [33], along with diverse nanostructure designs, enabling metalenses to achieve high transmission efficiency and functional integration across various wavelengths.

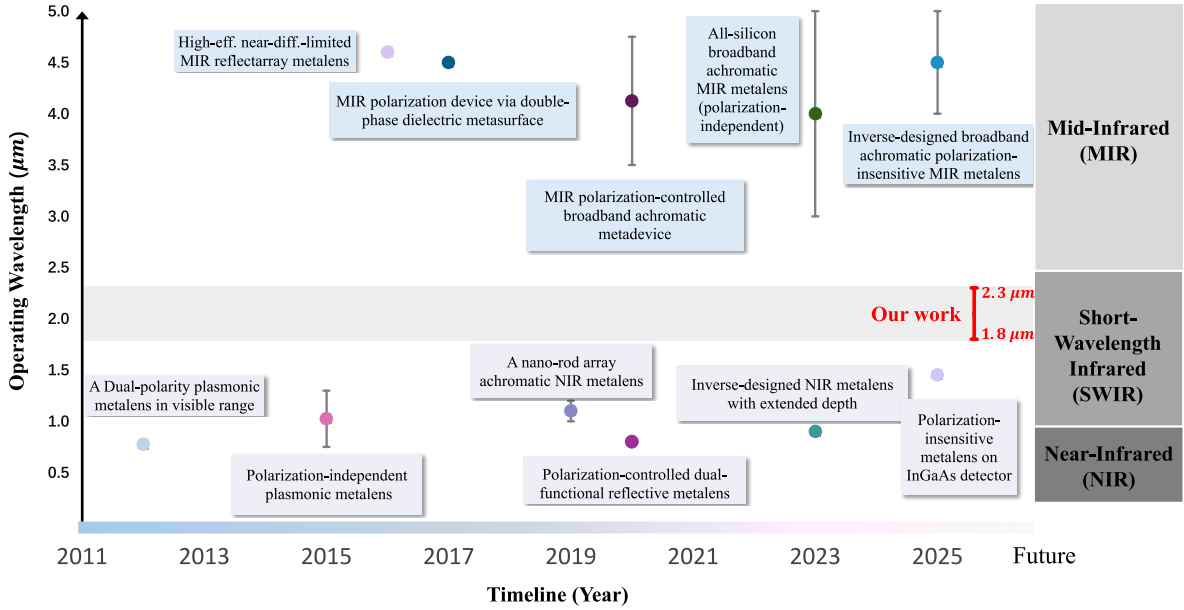


Fig. 1. Timeline of representative metalens developments across the near-infrared (NIR), short-wavelength infrared (SWIR), and mid-infrared (MIR) regions. Each point marks a key study identified by its publication year and operating wavelength. The error bars indicate the range of operating wavelengths, respectively. The diagram compiles results from multiple works [34–44]. Notably, fewer works have been reported in the SWIR band of 1.8–2.3 μm , which is the focus of this study.

These successive breakthroughs have not only facilitated the widespread integration of metalenses into conventional optical systems, but also gradually extended their application into the SWIR regime. Specifically, a number of devices operating around the telecommunication window [39, 45] (approximately 1.3–1.6 μm) have demonstrated functionalities such as focusing and polarization control. Meanwhile, increasing attention has been directed toward performance metrics including dispersion engineering and system-level integration [46, 47].

However, existing studies have primarily focused on narrowband or single-function optimization, leaving a gap in the development of SWIR optical devices that are both broadband and dispersion-engineered, as well as their integration solutions. This gap is particularly evident in the 1.8–2.3 μm range, a critical window bridging the near-infrared and mid-infrared regions. Despite its significant potential in quantum information transmission, nonlinear optics, and bridging near-IR to mid-IR applications, there remains a lack of systematic metalens designs and experimental validations in this band. To address this gap, we propose a broadband achromatic metalens operating in the 1.8–2.3 μm SWIR band. Compared to previous demonstrations such as [39] which employed multilayer intermediate structures including SiO_2 transition layers to achieve achromatic focusing, our design adopts a unified phase compensation strategy based on geometric and Pancharatnam-Berry (PB)-phase tuning. This simple structure not only improves fabrication efficiency but also facilitates integration with standard processes, thereby enhancing the scalability and practicality of the device across the SWIR band.

To the best of our knowledge, no prior work has demonstrated an achromatic metalens covering this entire spectral range. This is the first design study in this spectral window, providing

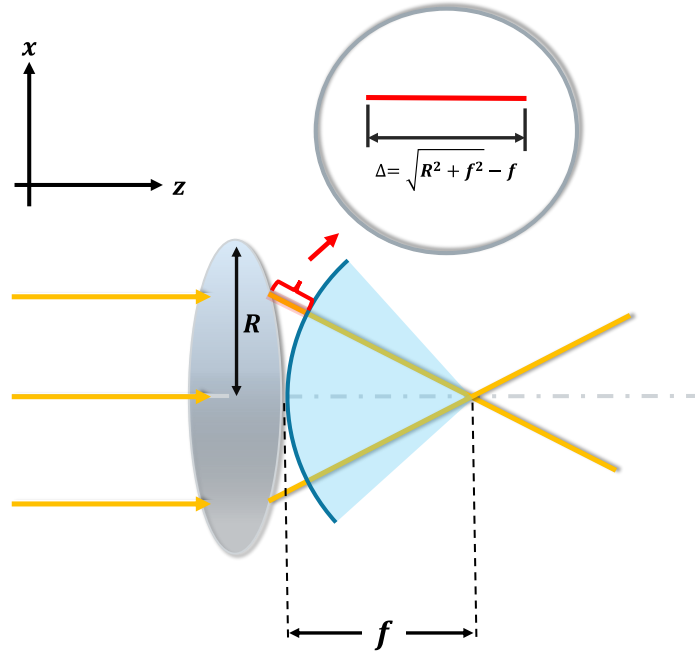


Fig. 2. Schematic diagram showing the ideal wavefront distribution for a metalens. To focus parallel incident light to a single focal point at distance f , the metasurface must introduce a spatially varying phase delay to compensate for the optical path difference between the center and off-axis positions. The required phase compensation at each radial distance R from the optical axis is given by $\Delta = \sqrt{R^2 + f^2} - f$, ensuring that all rays interfere constructively at the focus [49].

a pathway to balance achromaticity via geometric and PB-phase tuning. Most related works concentrate on a single, narrow-wavelength band, or limited-bandwidth performance, without offering integrated solutions that simultaneously provide broadband coverage, high efficiency, and dispersion compensation. This gap underscores the urgency and importance of conducting deeper investigations in this spectral range.

1.2. Basic Principle of Metalens

Based on subwavelength-scale nanostructure units, metalenses can precisely manipulate the phase, amplitude, and polarization state of light in space. By means of wavefront shaping and phase distribution design, metalenses enable effective control over light focusing, imaging performance, and dispersion characteristics. Compared with conventional optical lenses, metalenses overcome the limitations of bulk optics and enable integration by virtue of their ultrathin and compact structure. These advantages endow them with broad application potential in micro- and nano-optical systems. Benefiting from the high controllability of the geometry and spatial distribution of nano units, metalenses have become an important approach for designing multifunctional, high-performance optical components, and have been widely applied in fields such as achromatic imaging, super-resolution imaging, polarization manipulation, and multi-wavelength optical systems [30, 48, 49].

The focusing functionality of conventional lenses primarily relies on the geometrical thickness distribution across different radial positions, which introduces varying optical path lengths and consequently provides the necessary propagation phase compensation for the incident light.

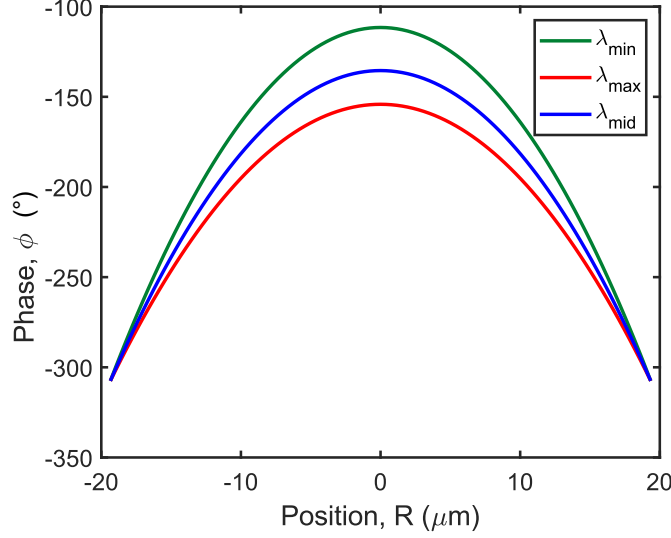


Fig. 3. Calculated phase distribution of the metalens along the radial direction for three different design wavelengths ($\lambda_{\min} = 1.8 \mu\text{m}$, $\lambda_{\text{mid}} = 2.05 \mu\text{m}$, and $\lambda_{\max} = 2.3 \mu\text{m}$). The curves indicate the required phase compensation to achieve focusing at the designed focal length, showing the variation of phase with respect to wavelength.

Through proper design, light waves from different positions accumulate appropriate phase delays, enabling constructive interference at the focal point and thus forming a clear focusing effect. In contrast, metalenses employ subwavelength-scale nano units to precisely manipulate the spatial phase distribution of the transmitted light, thereby actively shaping the wavefront. To achieve ideal focusing performance, the spatial phase at each position of the metalens must satisfy the following distribution (as shown in Fig. 2) [49]:

$$\varphi_{\text{ideal}}(R, \lambda) = -\frac{2\pi}{\lambda} \left(\sqrt{R^2 + f^2} - f \right), \quad (1)$$

Where R represents the radial position, with its unit determined by the specific design requirements. The parameter f denotes the designed focal length, and λ is the operating wavelength. Through precise manipulation of the geometric parameters of nanostructures, the output phase of individual unit cells can be effectively modulated, enabling continuous and controllable overall phase distributions. However, in practical metalens design, structural dispersion and local geometric constraints often lead to variation in the output phase with varying incident wavelengths. This makes it difficult to simultaneously match the required phase profiles at different wavelengths and significantly degrades the focusing performance and chromatic aberration suppression under broadband operation. Therefore, in addition to satisfying the phase requirements at a single wavelength, it is also essential to comprehensively consider the phase variation trends across different wavelengths, as illustrated in Fig. 3.

To address the aforementioned issues, this work applies a compensation design method, which involves introducing a wavelength-dependent compensation phase term [50]. This improves the overall phase consistency during the optimization process. This approach effectively suppresses phase deviations induced by dispersion and enhances the broadband focusing performance.

The phase compensation relationship at different wavelengths can be expressed as follows [51],

52]:

$$\varphi_{\text{lens}}(R, \lambda) = \varphi(R, \lambda_{\text{max}}) + \Delta\varphi(R, \lambda), \quad (2)$$

with a compensation phase:

$$\Delta\varphi(R, \lambda) = - \left[2\pi \left(\sqrt{R^2 + f^2} - f \right) \right] \left(\frac{1}{\lambda} - \frac{1}{\lambda_{\text{max}}} \right), \quad (3)$$

In the design of metalenses, the output phase imparted by each unit structure can typically be expressed as [51–54]:

$$\varphi_{\text{lens}}(R, \lambda) = \varphi_{\text{ideal}}(R, \lambda) + \Delta\varphi_{\text{struct}}(R, \lambda), \quad (4)$$

where $\Delta\varphi_{\text{struct}}(R, \lambda)$ represents the additional phase introduced by the specific meta-atom (including propagation and PB contributions).

Based on the wavelength-dependent output phase response of individual nano units, the following phase distribution needs to be constructed in practical design to meet the focusing requirements of the system at different wavelengths: The compensation phase is given by:

$$\Delta\varphi(R, \lambda) = - \left[2\pi \left(\sqrt{R^2 + f^2} - f \right) \right] \left(\frac{1}{\lambda} - \frac{1}{\lambda_{\text{max}}} \right) + C(\lambda), \quad (5)$$

where $C(\lambda)$ represents the optimized additional phase term for wavelength λ .

It is worth noting that the wavelength-dependent variation of this phase distribution essentially reflects the group delay (GD) characteristics of the system. Group delay describes the derivative of phase with respect to frequency (or wavelength), which can be expressed as:

$$\tau_g(R) = \frac{d\varphi(R, \lambda)}{d\omega} = - \frac{d\varphi(R, \lambda)}{d\lambda} \cdot \frac{d\lambda}{d\omega}, \quad (6)$$

$\tau_g(R)$ describes the time delay for different frequency components at position R . The output phase $\varphi(R, \lambda)$ depends on geometric path difference, structural dispersion, and PB phase. $\omega = 2\pi c/\lambda$ is the angular frequency, and the derivatives characterize phase and dispersion responses of the system.

Therefore, broadband metalens design requires not only static phase compensation at individual wavelengths, but also comprehensive consideration of the group delay distribution to ensure temporal consistency of the wavefront. By optimizing the structural parameters and compensation phase distribution, the group delay curve can be effectively flattened, thereby reducing focus shifts and wavefront distortions induced by dispersion, and ultimately achieving true broadband, high-quality imaging performance. The overall design approach enables broadband dispersion management and achromatic focusing, supporting consistent optical performance across the spectrum. However, the local tuning capability of geometric dimensions is inherently limited. As a result, relying solely on propagation phase compensation cannot fully satisfy the comprehensive design requirements of broadband metalenses, particularly in terms of wavefront consistency and chromatic aberration correction. To further enhance the overall phase control capability and dispersion suppression performance of the metalens under broadband operation, this work introduces the PB phase as an auxiliary phase modulation approach in the design.

The PB phase originates from the change in the polarization state of light, and essentially manifests as an additional phase introduced through the rotation of the nanostructure. Specifically,

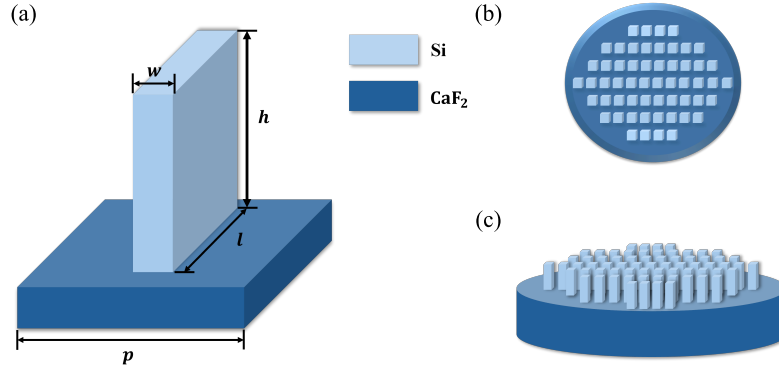


Fig. 4. Unitcell profile and structure of Metalens. (a) Schematic of the unit cell geometry used in the metalens design. The rectangular dielectric nanopillar has a length l , width w , and height h , and is placed on a dielectric substrate. (b) Top view of the metalens layout, showing the spatial arrangement of rectangular meta-atoms with varying geometries across the aperture. (c) Perspective view of the complete metalens composed of anisotropic nanopillars, where each unit is tailored to locally modulate the transmitted wavefront.

when incident circularly polarized light passes through an anisotropic unit structure, the corresponding transmission matrix can be expressed as:

$$t = \frac{t_L + t_S}{2} \begin{pmatrix} 1 \\ i \end{pmatrix} + \frac{t_L - t_S}{2} e^{i2\alpha} \begin{pmatrix} 1 \\ -i \end{pmatrix}, \quad (7)$$

where t_L and t_S represent the transmission coefficients of the structure along the long and short axes, respectively, and α denotes the rotation angle of the structure.

By adjusting the rotation angle α of the structure, controllable polarization-dependent phase compensation can be flexibly introduced without altering the overall dimensions or material parameters of the structure. The PB phase exhibits excellent broadband response and low dispersion characteristics, which effectively overcome the design limitations imposed by structural dispersion. In combination with propagation phase modulation, it significantly enhances the overall chromatic aberration compensation capability and wavefront control performance of the metalenses under broadband operation.

2. Design and Results

A single-bar nanocell structure based on silicon (Si) nanopillars on a calcium fluoride (CaF_2) substrate was designed to achieve efficient transmission modulation and precise phase control in the SWIR region. Calcium fluoride exhibits a low refractive index and excellent infrared transparency, while silicon offers a high refractive index and low absorption loss within this wavelength range. This material combination ensures a broad phase modulation range and stable focusing behavior over the operating bandwidth, while maintaining a reasonable transmission efficiency.

On the basis of the established material configuration, we systematically designed the nanocell geometry for left circularly polarized (LCP) input light. The unit cell period was set to $p = 900$ nm, and the pillar height was chosen as $h = 2 \mu\text{m}$ to minimize near-field coupling between adjacent elements and maintain wavefront shaping capability within the operating wavelength range. In addition, the nanocell length l was varied from 250 to 800 nm, while the width w was

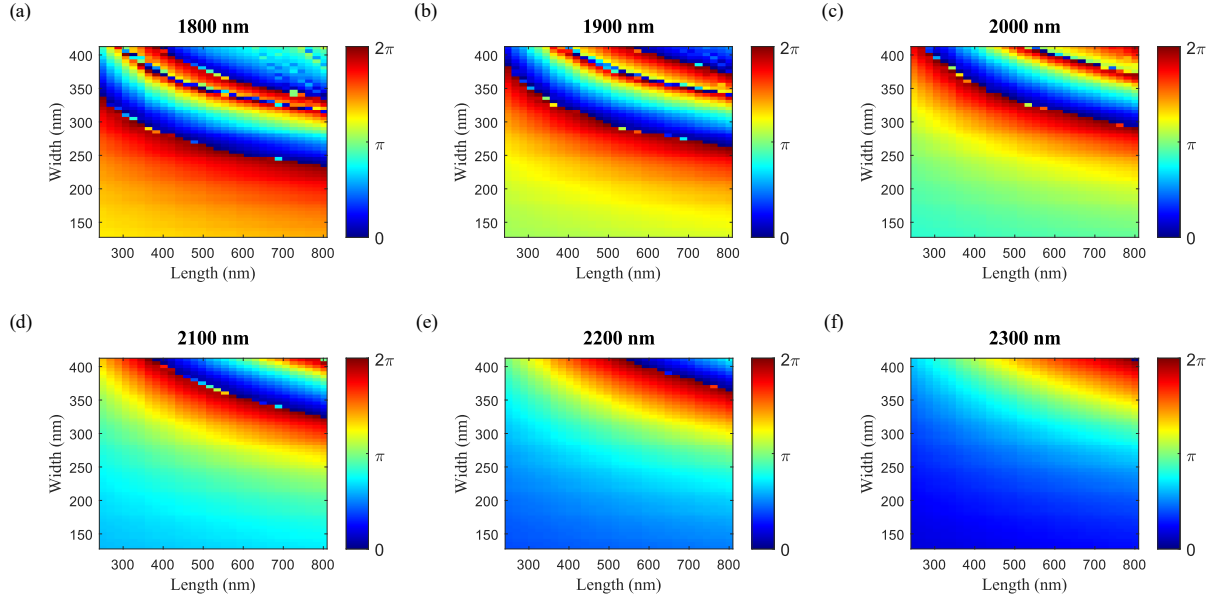


Fig. 5. Phase response maps of the unit cell under different wavelengths (1800 nm to 2300 nm). The phase distribution is plotted as a function of nanostructure length and width, showing a smooth phase variation across the SWIR band and achieving full $0-2\pi$ modulation.

tuned from 130 to 410 nm. Using the above approach, we carried out a multi-wavelength phase optimization. Specifically, we constructed a phase library via full-wave simulations for our nanocell across the geometry parameter space (l , w , θ) at the design wavelengths 1.8-2.3 μm . We then selected appropriate parameters for each radial position such that the phase condition Eq. (1) [with compensation Eq. (5)] is approximately satisfied for all wavelengths. This was followed by finetuning (e.g., θ) to improve broadband phase consistency. Geometric parameter tuning is combined with rotation-based phase modulation to achieve precise control of the transmitted wavefront. This approach enables the metalens to meet the design requirements for focusing and wavefront reconstruction. Fig. 4 illustrates the schematic of the proposed nanocell, its spatial arrangement within the metalens, and the overall three-dimensional structure of the device.

Subsequently, we further analyzed the transmission phase response of the designed nanocell in the target SWIR band to evaluate whether a complete 2π phase modulation can be achieved. Fig. 5 shows the simulated transmission phase distribution as a function of the nanocell length l and width w at different wavelengths (1800-2300 nm). The colors in the maps represent the phase delay provided by nanocells with different geometric dimensions. Within the designed parameter range ($l=250-800$ nm, $w=130-410$ nm), the nanocell provides a continuous phase coverage from 0 to 2π . The phase response remains smooth and continuous as the geometric dimensions are varied. Therefore, this structure can serve as a fundamental building block for broadband metalens devices, providing the foundation for the subsequent analysis and optimization of phase response and focus stability over a large wavelength range.

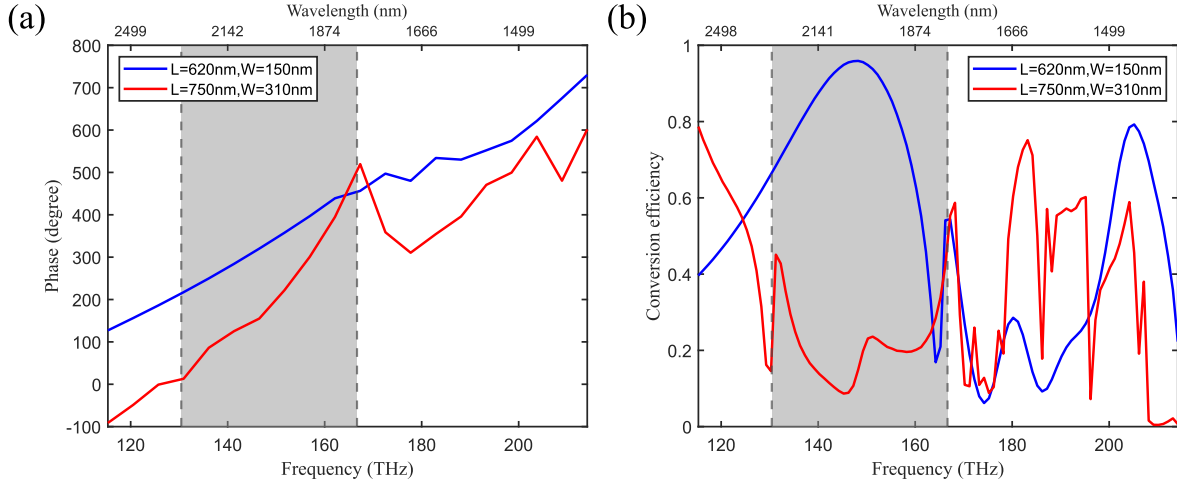


Fig. 6. Simulated phase response (a) and conversion efficiency (b) of rectangular dielectric nanopillars as functions of frequency for two sets of geometrical parameters ($L=620$ nm, $W=150$ nm and $L=750$ nm, $W=310$ nm). The shaded region highlights the target spectral range of 133-160 THz (1800-2300 nm).

To further assess the optical performance of the designed nanocells within the SWIR operating band, we conducted frequency-dependent simulations of their transmission phase response and the conversion efficiency from left-handed circularly polarized (LCP) light to right-handed circularly polarized (RCP) light. Fig. ?? displays the simulated phase delay and LCP→RCP conversion efficiency for two representative geometrical parameter sets ($L=620$ nm, $W=150$ nm and $L=750$ nm, $W=310$ nm) under different frequencies. The shaded region marks the target frequency range of 133-160 THz (corresponding to 1.8-2.3 μm). The results indicate that within this target band, the designed nanocells can achieve a relatively smooth and nearly linear phase variation trend. Meanwhile, the LCP→RCP conversion efficiency varies with geometry and frequency, providing useful insights for the optimization of subsequent devices in terms of phase control and polarization conversion.

We proceeded to analyze the PB phase characteristics of the designed structure. As demonstrated in Fig. 7, the transmission phase response was simulated under incident polarization angles of $\alpha = 0^\circ$, 30° , 60° , and 90° . The results show that the phase varies as a function of frequency for different polarization states over a broad range. This confirms the capability of the structure to achieve phase modulation based on the PB phase. Although the absolute phase levels differ among polarization angles, the overall phase–frequency curves remain nearly parallel, indicating a stable group delay trend. Minor variations in the phase slope appear around 160-170 THz (≈ 1.76 - 1.88 μm), indicating slight polarization-dependent dispersion in this range. It is noteworthy that these weak polarization-dependent dispersion effects are negligible and do not impose any practical limitation on employing the PB phase for phase distribution design and metalens optimization.

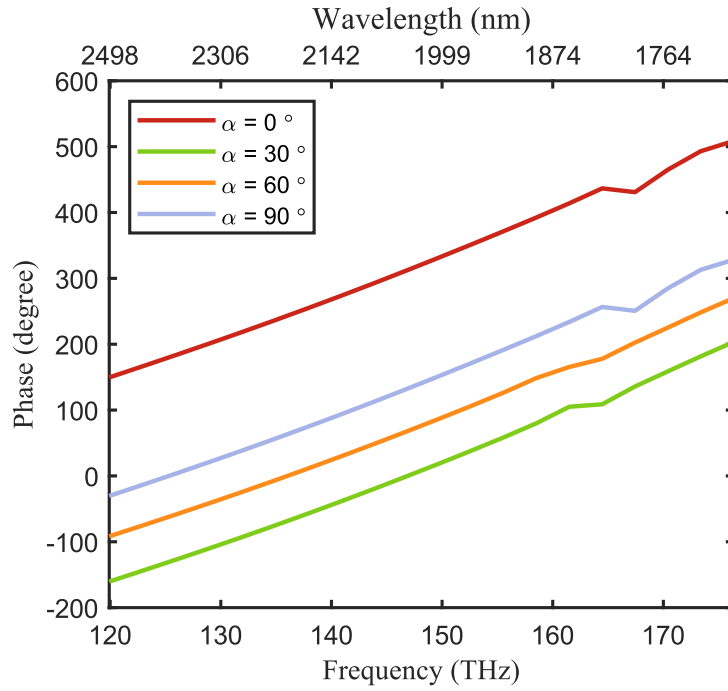


Fig. 7. Simulated transmission phase of the designed rectangular nanocell under different polarization angles ($\alpha = 0^\circ, 30^\circ, 60^\circ, 90^\circ$). The phase shows broadband frequency-dependent variation and nearly parallel trends across polarizations, indicating stable group delay and low polarization sensitivity. Slight slope changes near 160-170 THz (≈ 1.76 - $1.88 \mu\text{m}$) have negligible impact on phase design and metalens optimization.

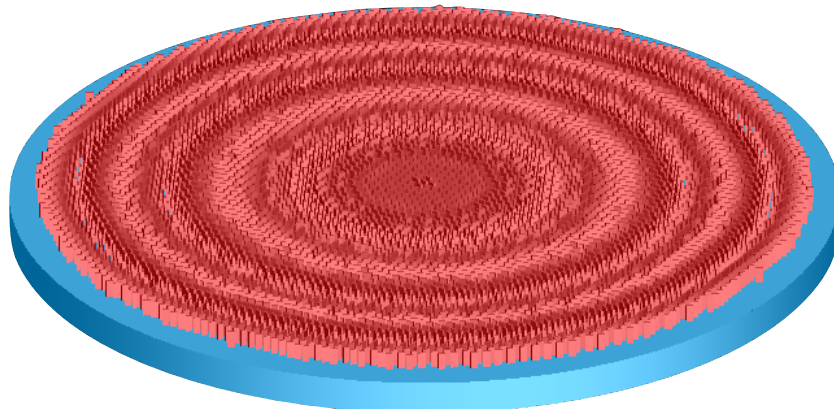


Fig. 8. Three-dimensional model of the designed silicon nanopillar metalens on a CaF_2 substrate, built in Lumerical FDTD. The device has an aperture radius of $R=38.7 \mu\text{m}$, a focal length of $f=100 \mu\text{m}$, and a numerical aperture of $\text{NA}=0.39$. This model serves as the basis for all subsequent FDTD simulations, including field distributions, focusing efficiency, and other performance analyses.

Based on the above material platform and the optimized nanocell parameters, we constructed a complete three-dimensional metalens model in Lumerical FDTD to evaluate its optical performance under realistic electromagnetic conditions. The metalens has an effective aperture radius of $R=38.7 \mu\text{m}$ and focal length of $f=100 \mu\text{m}$, corresponding numerical aperture of $\text{NA}=0.39$.

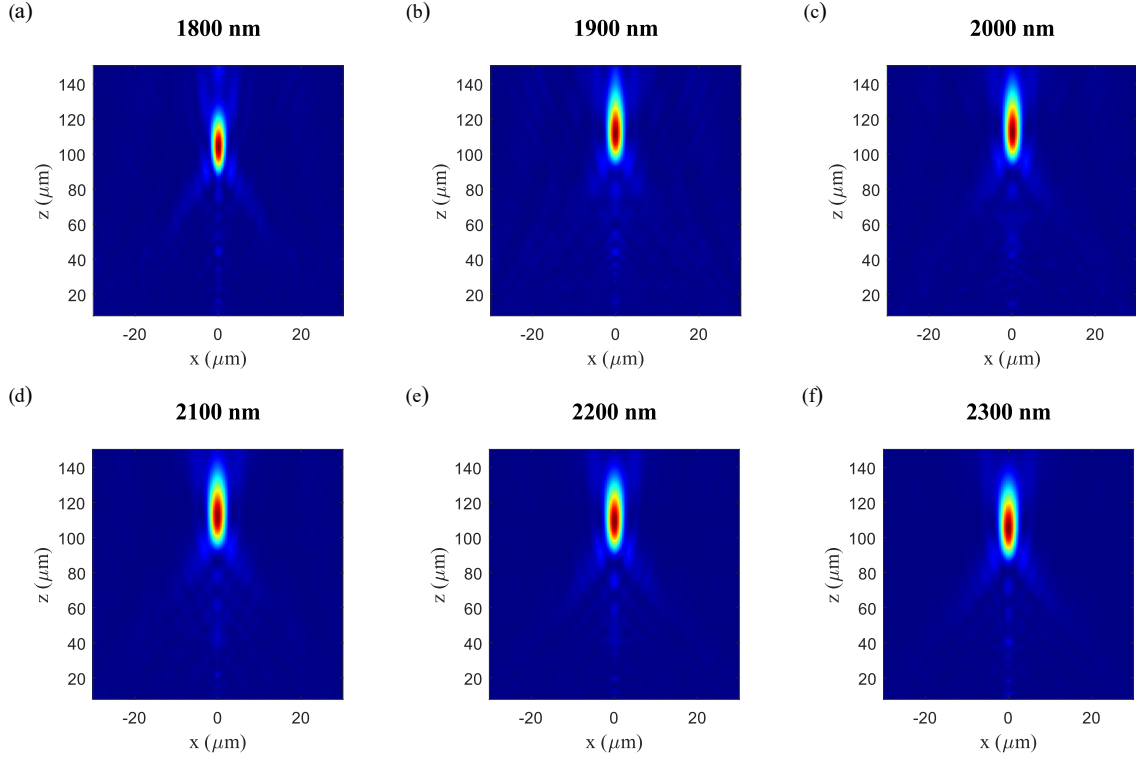


Fig. 9. Simulated electric field intensity distributions ($|E|^2$) in the X-Z plane at different wavelengths (1800-2300 nm) under normal incidence, indicating stable focal positioning across the spectral range.

The nanopillar elements are arranged on a square lattice with a period of $p=900$ nm, and each lattice site selects an appropriate geometry (l, w, θ) from the pre-established library according to the target focusing phase profile $\phi(r)$, thereby achieving the desired local transmission phase modulation. The 3D view of the complete model constructed in FDTD is shown in Fig. 8.

In order to evaluate the broadband focusing capability of the designed metalens, we simulated the electric field intensity distributions at different wavelengths (1800-2300 nm), as shown in Fig. 9. These figures present the normalized electric field intensity ($|E|^2$) distributions in the X-Z plane under normal incidence. It can be observed that, throughout the short-wave infrared band, the focal spots exhibit strong energy confinement and remain stably located at the designed focal length of $100 \mu\text{m}$, with longitudinal focal shifts within 6% ($\pm 6 \mu\text{m}$) of the target value. Specifically, the focal length varies from $100 \mu\text{m}$ at $\lambda = 1800$ nm to $105.8 \mu\text{m}$ at $\lambda = 2300$ nm, based on the simulation results. Although the wavelength varies significantly, the focusing profiles remain laterally stable. This suggests that the structure provides effective phase matching and chromatic aberration correction. No significant lateral chromatic aberration was observed across the wavelength range, as the focal spot consistently remained centered on the optical axis. In addition, the focal spot size quantified by the FWHM of the intensity distribution exhibited only minimal variation and remained nearly constant from 1800 nm to 2300 nm.

Based on the preceding analysis, the focusing efficiency of the metalens at different wavelengths was evaluated, as presented in Fig. 10. Focusing efficiency is defined as the ratio of the effectively focused energy within the focal plane region (calculated within a radius of $1.5 \times \text{FWHM}$ from the optical axis at the focal plane) to the total transmitted energy, reflecting the degree of spatial energy confinement at the focal point. The results show that the focusing

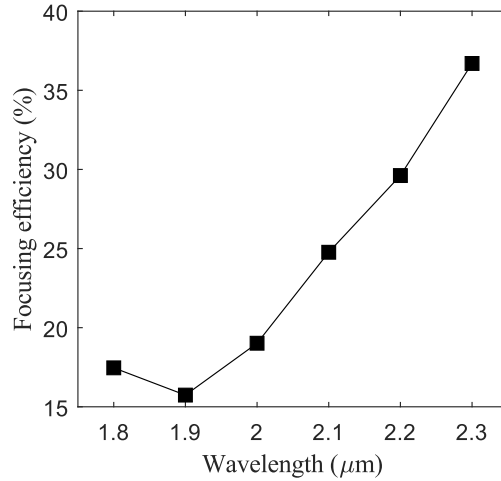


Fig. 10. Simulated focusing efficiency of the metalens as a function of wavelength from $1.8 \mu\text{m}$ to $2.3 \mu\text{m}$. The efficiency increases gradually with wavelength, reaching approximately 38% at $2.3 \mu\text{m}$. The trend indicates improved focusing performance at longer wavelengths within the SWIR band.

efficiency remains moderate (e.g., 20-38%) across the 1800-2300 nm range and shows a gradual increase with wavelength. This performance indicates that the device maintains a reasonable degree of energy confinement given the broad bandwidth and achromatic design requirements. In other words, achromatic focusing is achieved at the cost of some efficiency trade-off, which is a commonly observed balance in broadband metalens systems.

For clarity in evaluating the polarization control capability of the structure across different wavelengths, Fig. 11 shows the polarization state distributions of the output light on the Poincaré sphere together with the corresponding degree of polarization (DoP). In the figure, the red vectors represent the directions of the output Stokes vectors, while the blue dots denote their endpoints. The DoP values are used to quantify the purity of the output polarization state. As shown, the DoP remains within 0.42-0.50 in the 1800-2000 nm range, indicating relatively concentrated polarization states. However, as the wavelength approaches 2300 nm, the DoP decreases significantly, reaching a minimum of 0.06, which indicates a substantial reduction in polarization purity.

This phenomenon can be attributed to the wavelength-dependent phase retardation of the anisotropic nanostructures used in the PB-phase mechanism. At longer wavelengths near 2300 nm, the phase shift between orthogonal polarization components deviates from the ideal π radians, resulting in incomplete polarization conversion and reduced DoP. This suggests that the structure's polarization response has a limited operational bandwidth, although the exact mechanism may require further investigation.

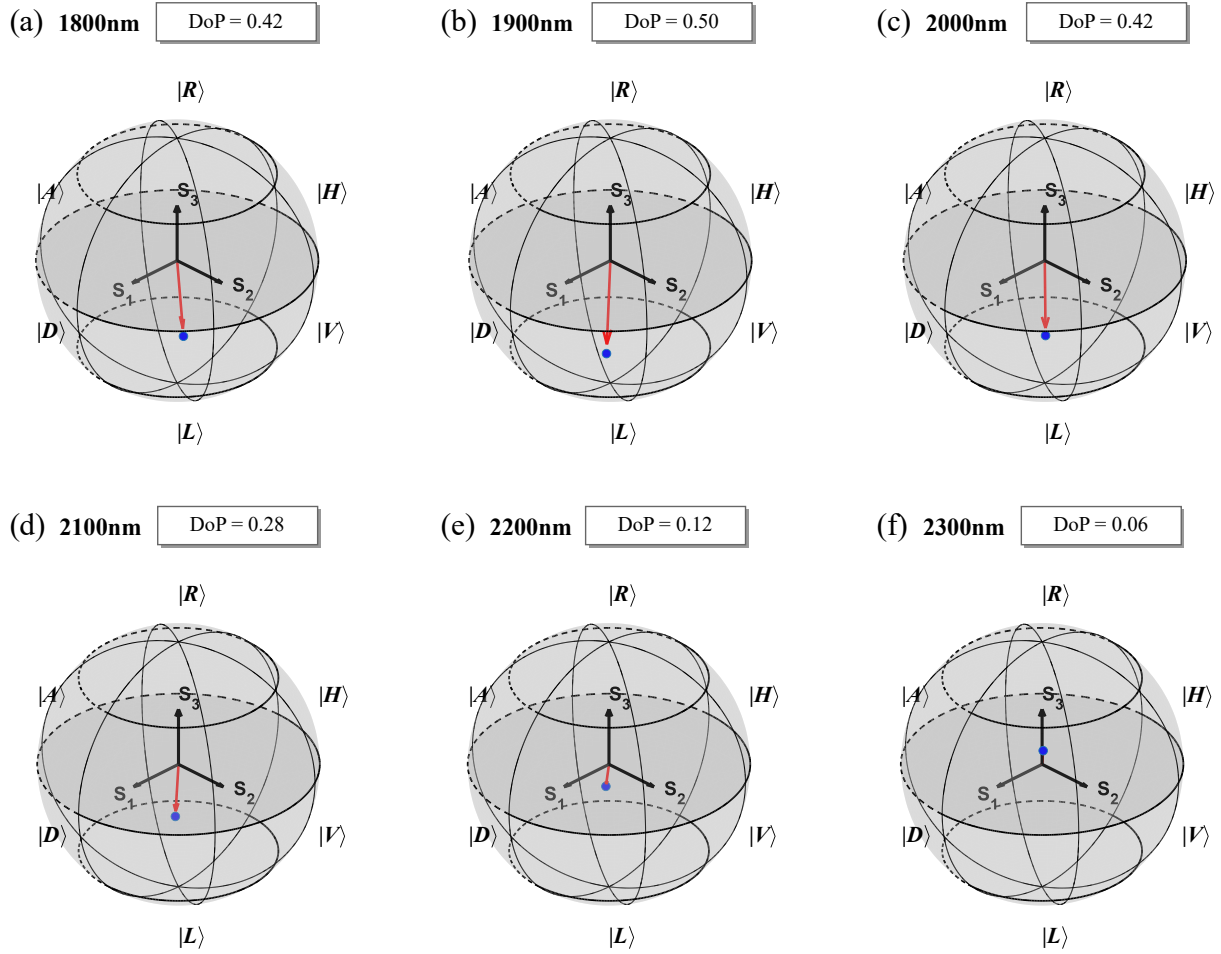


Fig. 11. Simulated polarization states at the focal point visualized on the Poincaré sphere for wavelengths from 1800 nm to 2300 nm. Each red arrow represents the normalized Stokes vector of the focal-field polarization state, and the corresponding degree of polarization (DoP) is labeled beside each sphere.

Focusing on the overall spectral performance of the metalens, Fig. 12 illustrates the variation trends of total power transmitted through the metalens (regardless of focus) and the polarization purity (DoP) at the focal spot at different wavelengths, aiming to explore the trade-off between these two performance metrics. It can be observed that the transmission remains at a high level across the 1.8–2.3 μm wavelength range and slightly increases with wavelength, reaching a maximum of nearly 83%. In contrast, the DoP shows a gradual decline as the wavelength increases. This is likely because the nanopillars are designed to impart a π phase difference (half-wave retardation) between fast and slow axes around the mid-band. At the extreme of 2.3 μm , the phase difference might deviate significantly from π , resulting in incomplete conversion and a mix of polarizations at focus. It approaches zero at the long-wavelength end, showing a significant degradation of polarization purity.

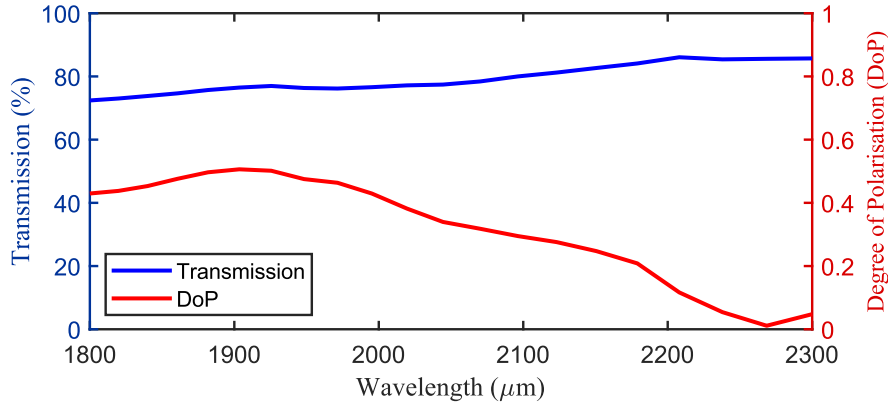


Fig. 12. Simulated transmission (blue curve, left axis) and DoP (red curve, right axis) of the allband metalens across the 1800-2300 nm wavelength range. The results reveal a trade-off between achieving high transmission and preserving polarization purity across the spectrum.

This trend suggests that the current structure can achieve high transmission but has limited capability in preserving polarization. Such behavior reflects a typical trade-off between transmission efficiency and polarization control. This phenomenon may be attributed to the inconsistent response of the meta-atoms to different wavelengths and polarization directions. The high overall transmission (reaching 83%) across the band indicates low losses; thus the reduced focusing/polarization performance at the edges is due to phase control limitations rather than loss. These results further highlight that, in broadband metalens design, achieving a balance between high transmittance and effective polarization control remains a critical challenge that must be addressed in future optimization efforts. Future efforts could explore multi-layer metasurfaces or novel geometries to maintain polarization control across broad bandwidths, potentially alleviating this trade-off.

While this study is based on numerical simulations, the proposed metalens design has been carefully considered to ensure compatibility with current nanofabrication capabilities. The minimum feature width (~ 130 nm) lies within the capabilities of current nanofabrication techniques, such as electron-beam lithography or deep-UV lithography [55]. The high aspect ratio (up to approximately 13:1, given a $2 \mu\text{m}$ height) poses a known challenge, but previous works have demonstrated similar structures are achievable [56, 57]. In terms of material compatibility, the Si-on- CaF_2 platform offers both low-loss optical performance in the SWIR band and reasonable process compatibility, although additional support (e.g., carrier wafers) may be required during fabrication [58]. These factors collectively support the experimental feasibility of the proposed structure. Moreover, although no dedicated tolerance simulation is performed in this study, previous works have demonstrated that metasurface-based devices, including achromatic metalenses, can maintain robust performance under moderate fabrication deviations [59, 60]. These results support the general tolerance of such nanostructures to typical fabrication imperfections, reinforcing the practical feasibility of the proposed design.

Conclusion

This study presents, to the best of our knowledge, the first proposal and numerical validation of a broadband achromatic metalens operating in the 1800-2300 nm short-wave infrared (SWIR)

band, constructed from a Si nanopillar array on a CaF₂ substrate. By combining geometric tuning with Pancharatnam–Berry (PB) phase engineering, continuous 2π phase modulation is achieved. The designed structure exhibits a stable focal ability, broad operating range capability, and low lateral aberrations across the entire operating band. The polarization analysis further demonstrates that as the wavelength increases, the DoP at the focal point shows a gradual downward trend. This indicates that while the structure enhances transmission efficiency, its polarization retention capability faces challenges, reflecting a potential performance trade-off between polarization purity and transmission efficiency. This observation provides valuable guidance for future optimization of polarization control. Overall, the results offer strong support for the design of structures that simultaneously achieve broadband achromaticity, high transmission efficiency, and polarization control on integrated photonic platforms, although trade-offs between these metrics remain. This work provides valuable design guidelines and a foundation for advanced photonic systems in the SWIR band that require spectral manipulation with reasonable transmission and focusing efficiencies. Future optimizations could build on this work to further improve polarization purity while maintaining broadband performance. More work is needed to experimentally validate the proposed design, including fabrication and characterization of its broadband focusing and polarization performance.

Acknowledgements: This work was supported in part by the Royal Society (Grant No. RG\R1\251474). We thank Natale Pruiti and Marc Sorel for their support with Lumerical simulations, and Shuhao Wu, Miles Padgett for helpful discussions.

References

1. J. C. Mars and L. C. Rowan, “Spectral assessment of new aster swir surface reflectance data products for spectroscopic mapping of rocks and minerals,” *Remote. Sens. Environ.* **114**, 2011–2025 (2010).
2. A. Campargue, S. N. Mikhailenko, S. Vasilchenko, C. Reynaud, S. Béguier, P. Čermák, D. Mondelain, S. Kassi, and D. Romanini, “The absorption spectrum of water vapor in the 2.2 μm transparency window: High sensitivity measurements and spectroscopic database,” *J. Quant. Spectrosc. Radiat. Transf.* **189**, 407–416 (2017).
3. N. Pahlevan, J. Claude Roger, Z. Ahmad, H. R. Gordon, and M. Wang, “Revisiting short-wave-infrared (swir) bands for atmospheric correction in coastal waters,” *Opt. Express*, Vol. 25, Issue 6, pp. 6015–6035 **25**, 6015–6035 (2017).
4. E. Knaeps, K. G. Ruddick, D. Doxaran, A. I. Dogliotti, B. Nechad, D. Raymaekers, and S. Sterckx, “A swir based algorithm to retrieve total suspended matter in extremely turbid waters,” *Remote. Sens. Environ.* **168**, 66–79 (2015).
5. E. Pugliese, M. Locatelli, R. Meucci, S. Euzzor, and P. Poggi, “Swir digital holography and imaging through smoke and flames: unveiling the invisible,” *Opt. Express*, Vol. 31, Issue 25, pp. 42090–42098 **31**, 42090–42098 (2023).
6. B. Stark, M. McGee, and Y. Chen, “Short wave infrared (swir) imaging systems using small unmanned aerial systems (suas),” 2015 Int. Conf. on Unmanned Aircr. Syst. ICUAS 2015 pp. 495–501 (2015).
7. A. Bessonov, A. Rozanov, R. White, G. Suwito, I. Medina-Salazar, M. Lutfullin, D. Gusev, and I. Shikov, “All-weather drone vision: Passive swir imaging in fog and rain,” *Drones* 2025, Vol. 9, Page 553 **9**, 553 (2025).
8. M. Wen, L. Wei, X. Zhuang, D. He, S. Wang, and Y. Wang, “High-sensitivity short-wave infrared technology for thermal imaging,” *Infrared Phys. & Technol.* **95**, 93–99 (2018).
9. A. Attiaoui, É. Bouthillier, G. Daligou, A. Kumar, S. Assali, and O. Moutanabbir, “Extended short-wave infrared absorption in group iv nanowire arrays,” *Phys. Rev. Appl.* **15** (2020).

10. S. Sarkar, P. Le, J. Geng, Y. Liu, Z. Han, M. U. Zahid, D. Nall, Y. Youn, P. R. Selvin, and A. M. Smith, "Short-wave infrared quantum dots with compact sizes as molecular probes for fluorescence microscopy," *J. Am. Chem. Soc.* **142**, 3449 (2020).
11. J. Leemans, V. P. Pejović, E. Georgitzikis, M. Minjauw, A. B. Siddik, Y.-H. Deng, Y. Kuang, G. Roelkens, C. Detavernier, I. Lieberman, P. E. Malinowski, D. Cheyns, Z. Hens, J. Leemans, Y.-H. Deng, Z. Hens, V. P. Pejović, E. Georgitzikis, A. B. Siddik, Y. Kuang, I. Lieberman, P. E. Malinowski, D. Cheyns, M. Minjauw, C. Detavernier, and G. Roelkens, "Colloidal iii-v quantum dot photodiodes for short-wave infrared photodetection," *Adv. Sci.* **9**, 2200844 (2022).
12. R. H. Wilson, K. P. Nadeau, F. B. Jaworski, B. J. Tromberg, and A. J. Durkin, "Review of short-wave infrared spectroscopy and imaging methods for biological tissue characterization," *J. Biomed. Opt.* **20**, 030901 (2015).
13. J. A. Gutiérrez-Gutiérrez, V. Mieites, J. M. López-Higuera, and O. M. Conde, "Rotating mirror short-wave infrared hyperspectral imaging system: Characterization and applications," *Sensors Actuators B: Chem.* **439**, 137762 (2025).
14. F. J. A. van Ruitenbeek, W. H. Bakker, H. M. A. van der Werff, C. A. Hecker, K. A. A. Hein, and W. van Eijndthoven, "A knowledge-based strategy for interpretation of swir hyperspectral images of rocks," *Remote. Sens.* 2025, Vol. 17, Page 2555 **17**, 2555 (2025).
15. M. Mehrubeoglu, A. V. Sickle, and J. Turner, "Detection and identification of plastics using swir hyperspectral imaging," (*SPIE-Intl Soc Optical Eng*, 2020), p. 15.
16. B. Keizers, T. S. Nijboer, C. A. M. van der Fels, M. C. van den Heuvel, G. M. van Dam, S. Kruijff, I. J. de Jong, M. J. H. Witjes, F. J. Voskuil, D. Gorpas, W. R. Browne, and P. J. van der Zaag, "Systematic comparison of fluorescence imaging in the near-infrared and shortwave-infrared spectral range using clinical tumor samples containing cetuximab-irdye800cw," *J. Biomed. Opt.* **30**, S13708 (2024).
17. C. Yao, R. Wei, X. Luo, J. Zhou, X. Zhang, X. Lu, Y. Dong, R. Chu, Y. Sun, Y. Wang, W. Xia, D. Qu, C. Liu, J. Ren, G. Ge, J. Chen, X. Qian, and Y. Yang, "A stable and biocompatible short-wave infrared nanoribbon for dual-channel in vivo imaging," *Nat. Commun.* **16**, 1–12 (2025).
18. M. Abuzar, K. Sheffield, and A. McAllister, "Feasibility of using swir-transformed reflectance (str) in place of surface temperature (ts) for the mapping of irrigated landcover," *Land* 2024, Vol. 13, Page 633 **13**, 633 (2024).
19. C. W. Golden, R. Griffin, W. Schroder, K. Herndon, J. Casana, and C. Ferwerda, "Drone-acquired short-wave infrared (swir) imagery in landscape archaeology: An experimental approach," *Remote. Sens.* 2024, Vol. 16, Page 1671 **16**, 1671 (2024).
20. S. L. Ustin and E. M. P. Middleton, "Current and near-term earth-observing environmental satellites, their missions, characteristics, instruments, and applications," *Sensors (Basel, Switzerland)* **24**, 3488 (2024).
21. D. J. Jacob, D. J. Varon, D. H. Cusworth, P. E. Dennison, C. Frankenberg, R. Gautam, L. Guanter, J. Kelley, J. McKeever, L. E. Ott, B. Poulter, Z. Qu, A. K. Thorpe, J. R. Worden, and R. M. Duren, "Quantifying methane emissions from the global scale down to point sources using satellite observations of atmospheric methane," *Atmospheric Chem. Phys.* **22**, 9617–9646 (2022).
22. J. L. Gach, D. Boutolleau, C. Brun, T. Carmignani, F. Clop, P. Feautrier, S. Lemarchand, E. Stadler, and Y. Wanwanscappel, "C-red 3: A swir camera for fso applications," (2020).
23. S. Hearne, J. Horgan, N. Boujnah, and D. Kilbane, "Wavelength selection for satellite quantum key distribution," *Appl. Sci.* 2025, Vol. 15, Page 1308 **15**, 1308 (2025).
24. S. Prabhakar, T. Shields, A. C. Dada, M. Ebrahim, G. G. Taylor, D. Morozov, K. Erotokritou, S. Miki, M. Yabuno, H. Terai, C. Gawith, M. Kues, L. Caspani, R. H. Hadfield, and M. Clerici, "Two-photon quantum interference and entanglement at 2.1 μm ," *Sci. Adv.* **6**, 5195–5222 (2020).
25. A. Orioux and E. Diamanti, "Recent advances on integrated quantum communications," *J. Opt.* **18**, 083002 (2016).
26. S. Pirandola, S. Pirandola, U. L. Andersen, L. Banchi, M. Berta, D. Bunandar, R. Colbeck, D. En-

- glund, T. Gehring, C. Lupo, C. Ottaviani, J. L. Pereira, M. Razavi, J. S. Shaari, J. S. Shaari, M. Tomamichel, M. Tomamichel, V. C. Usenko, G. Vallone, P. Villoresi, and P. Wallden, “Advances in quantum cryptography,” *Adv. Opt. Photonics*, Vol. 12, Issue 4, pp. 1012–1236 **12**, 1012–1236 (2020).
27. H. C. V. Tran, E. Jang, J. Kim, M. Choi, Y. Park, H. Jeong, T. Goo, S. Bae, and S. Jeong, “Enhanced swir photodetection in colloidal quantum dot photodiodes via tunneling current suppression,” *ACS Appl. Mater. & Interfaces* **17**, 15666–15674 (2025).
 28. S. Bianconi and H. Mohseni, “Recent advances in infrared imagers: Toward thermodynamic and quantum limits of photon sensitivity,” *Reports on progress physics. Phys. Soc. (Great Britain)* **83**, 044101 (2020).
 29. M. Khorasaninejad and F. Capasso, “Metalenses: Versatile multifunctional photonic components,” *Science* **358** (2017).
 30. A. Arbabi, Y. Horie, M. Bagheri, and A. Faraon, “Dielectric metasurfaces for complete control of phase and polarization with subwavelength spatial resolution and high transmission,” *Nat. Nanotechnol.* **10**, 937–943 (2015).
 31. H. Liang, Q. Lin, X. Xie, Q. Sun, Y. Wang, L. Zhou, L. Liu, X. Yu, J. Zhou, T. F. Krauss, and J. Li, “Ultrahigh numerical aperture metalens at visible wavelengths,” *Nano Lett.* **18**, 4460–4466 (2018).
 32. L. Huang, Z. Coppens, K. Hallman, Z. Han, K. F. Böhringer, N. Akozbek, A. Raman, A. Majumdar, and A. Majumdar, “Long wavelength infrared imaging under ambient thermal radiation via an all-silicon metalens,” *Opt. Mater. Express*, Vol. 11, Issue 9, pp. 2907–2914 **11**, 2907–2914 (2021).
 33. B. H. Chen, P. C. Wu, V. C. Su, Y. C. Lai, C. H. Chu, I. C. Lee, J. W. Chen, Y. H. Chen, Y. C. Lan, C. H. Kuan, and D. P. Tsai, “Gan metalens for pixel-level full-color routing at visible light,” *Nano Lett.* **17**, 6345–6352 (2017).
 34. X. Chen, L. Huang, H. Mühlenbernd, G. Li, B. Bai, Q. Tan, G. Jin, C. W. Qiu, S. Zhang, and T. Zentgraf, “Dual-polarity plasmonic metalens for visible light,” *Nat. Commun.* **3**, 1–6 (2012).
 35. W. Wang, Z. Guo, R. Li, J. Zhang, Y. Li, Y. Liu, X. Wang, S. Qu, L. Verslegers, P. B. Catrysse, Z. Yu, J. S. White, E. S. Barnard, M. L. Brongersma, S. Fan, H. Gao, J. K. Hyun, M. H. Lee, J. C. Yang, L. J. Lauhon, and T. W. Odom, “Plasmonics metalens independent from the incident polarizations,” *Opt. Express*, Vol. 23, Issue 13, pp. 16782–16791 **23**, 16782–16791 (2015).
 36. B. Yu, J. Wen, X. Chen, and D. Zhang, “An achromatic metalens in the near-infrared region with an array based on a single nano-rod unit,” *Appl. Phys. Express* **12**, 092003 (2019).
 37. Y. Zhang, B. Yang, Z. Liu, and Y. Fu, “Polarization controlled dual functional reflective planar metalens in near infrared regime,” *Coatings 2020*, Vol. 10, Page 389 **10**, 389 (2020).
 38. S. Xiao, S. Xiao, F. Zhao, D. Wang, J. Weng, J. Weng, Y. Wang, X. He, H. Chen, Z. Zhang, Y. Yu, Z. Zhang, Z. Zhang, Z. Zhang, J. Yang, and J. Yang, “Inverse design of a near-infrared metalens with an extended depth of focus based on double-process genetic algorithm optimization,” *Opt. Express*, Vol. 31, Issue 5, pp. 8668–8681 **31**, 8668–8681 (2023).
 39. Y. Zou, Y. Xu, and M. Fang, “Broadband polarisation-insensitive metalens design with easy functionality expansion on an ingaas-detector substrate off-chip,” *SSRN Prepr. p. ssrn.5221467* (2025).
 40. S. Zhang, M. hwan Kim, F. Aieta, A. She, T. Mansuripur, I. Gabay, M. Khorasaninejad, D. Rousso, X. Wang, M. Troccoli, F. Capasso, N. Yu, P. Genevet, F. Aieta, M. A. Kats, R. Blanchard, G. Aoust, J. P. Tetienne, Z. Gaburro, F. Capasso, A. Kats, M. Khorasaninejad, W. T. Chen, R. C. Devlin, J. Oh, and A. Y. Zhu, “High efficiency near diffraction-limited mid-infrared flat lenses based on metasurface reflectarrays,” *Opt. Express*, Vol. 24, Issue 16, pp. 18024–18034 **24**, 18024–18034 (2016).
 41. Z. Guo, L. Tian, F. Shen, H. Zhou, and K. Guo, “Mid-infrared polarization devices based on the double-phase modulating dielectric metasurface,” *J. Phys. D: Appl. Phys.* **50**, 254001 (2017).
 42. K. Ou, F. Yu, G. Li, W. Wang, A. E. Miroschnichenko, L. Huang, P. Wang, T. Li, Z. Li, X. Chen,

- and W. Lu, "Mid-infrared polarization-controlled broadband achromatic metadvice," *Sci. Adv.* **6**, 711–722 (2020).
43. S. Yue, S. Yue, S. Yue, Y. Liu, Y. Liu, R. Wang, R. Wang, Y. Hou, Y. Hou, H. Shi, H. Shi, Y. Feng, Y. Feng, Z. Wen, Z. Wen, Z. Zhang, and Z. Zhang, "All-silicon polarization-independent broadband achromatic metalens designed for the mid-wave and long-wave infrared," *Opt. Express*, Vol. 31, Issue 26, pp. 44340–44352 **31**, 44340–44352 (2023).
 44. S. Xu, P. Kang, J. Chen, Z. Hu, W. Chang, and F. Huang, "Inverse design broadband achromatic and polarizations-insensitive metalens in mid-infrared," *Opt. Commun.* **579**, 131586 (2025).
 45. K. Liu, C. Sun, and H. C. Chui, "Telecom-band high contrast narrowband metalens for 3d imaging," *Opt. Lasers Eng.* **180**, 108325 (2024).
 46. F. Zhang, H. Bao, M. Pu, Y. Guo, T. Kang, X. Li, Q. He, M. Xu, X. Ma, and X. Luo, "Dispersion-engineered spin photonics based on folded-path metasurfaces," *Light. Sci. Appl.* **14**, 1–10 (2025).
 47. Y. Zhang, X. Jiang, G. Qu, J. Han, C. Li, B. Bo, Q. Ruan, Z. Liu, Q. Song, and S. Xiao, "On-chip integration of achromatic metalens arrays," *Nat. Commun.* **16**, 1–8 (2025).
 48. Y. Wang, Q. Chen, W. Yang, Z. Ji, L. Jin, X. Ma, Q. Song, A. Boltasseva, J. Han, V. M. Shalaev, and S. Xiao, "High-efficiency broadband achromatic metalens for near-ir biological imaging window," *Nat. Commun.* **12**, 1–7 (2021).
 49. W. T. Chen, A. Y. Zhu, V. Sanjeev, M. Khorasaninejad, Z. Shi, E. Lee, and F. Capasso, "A broadband achromatic metalens for focusing and imaging in the visible," *Nat. Nanotechnol.* **13**, 220–226 (2018).
 50. F. Aieta, M. A. Kats, P. Genevet, and F. Capasso, "Multiwavelength achromatic metasurfaces by dispersive phase compensation," *Science* **347**, 1342–1345 (2015).
 51. S. Wang, P. C. Wu, V. C. Su, Y. C. Lai, M. K. Chen, H. Y. Kuo, B. H. Chen, Y. H. Chen, T. T. Huang, J. H. Wang, R. M. Lin, C. H. Kuan, T. Li, Z. Wang, S. Zhu, and D. P. Tsai, "A broadband achromatic metalens in the visible," *Nat. Nanotechnol.* **13**, 227–232 (2018).
 52. K. Guo, C. Wang, Q. Kang, L. Chen, and Z. Guo, "Broadband achromatic metalens with polarization insensitivity in the mid-infrared range," *Opt. Mater.* **131**, 112489 (2022).
 53. Y. Zhang, X. Jiang, G. Qu, J. Han, C. Li, B. Bo, Q. Ruan, Z. Liu, Q. Song, and S. Xiao, "On-chip integration of achromatic metalens arrays," *Nat. Commun.* **16**, 1–8 (2025).
 54. W. T. Chen, A. Y. Zhu, J. Sisler, Z. Bharwani, and F. Capasso, "A broadband achromatic polarization-insensitive metalens consisting of anisotropic nanostructures," *Nat. Commun.* **10**, 1–7 (2019).
 55. V. R. Manfrinato, J. Wen, L. Zhang, Y. Yang, R. G. Hobbs, B. Baker, D. Su, D. Zakharov, N. J. Zaluzec, D. J. Miller, E. A. Stach, and K. K. Berggren, "Determining the resolution limits of electron-beam lithography: Direct measurement of the point-spread function," *Nano Lett.* **14**, 4406–4412 (2014).
 56. T. Duan, C. Gu, D. S. Ang, K. Xu, and Z. Liu, "A novel fabrication technique for high-aspect-ratio nanopillar arrays for sers application," *RSC Adv.* **10**, 45037–45041 (2020).
 57. A. Pan, M. Samaan, Z. Yan, W. Hu, B. Cui, J. B. V. S. Technol, and B. C. AFFILIATIONS, "Fabrication of ultrahigh aspect ratio si nanopillar and nanocone arrays," *J. Vac. Sci. & Technol. B* **41**, 23001 (2023).
 58. Q. Song, J. Cai, C. Wang, L. Zhou, Y. Chen, M. Zhou, J. Zhang, B. Yang, Y. Yang, A. Yi, T. You, and X. Ou, "Wafer-scale fabrication of single-crystalline calcium fluoride thin-film on insulator by ion-cutting," *Opt. Mater.* **157**, 115787 (2024).
 59. H. C. Wang, K. Achouri, and O. J. Martin, "Robustness analysis of metasurfaces: Perfect structures are not always the best," *ACS Photonics* **9**, 2438–2447 (2022).
 60. Y. Qiu, L. Deng, Y. Zhan, G. Li, and J. Guan, "The effect of height error on performance of propagation phase-based metalens," *Micromachines* 2024, Vol. 15, Page 540 **15**, 540 (2024).